Stretchable Electronic Skin Using Laser-Induced Graphene and Liquid Metal With an Action Recognition System Powered by Machine Learning

*Yanpeng Li, Guren Matsumura, Yan Xuan, Satoko Honda, Kuniharu Takei**

Y. Li, Y. Xuan, K. Takei

Graduate School of Information Science and Technology, Hokkaido University, Sapporo, Hokkaido 060-0814, Japan

takei@ist.hokudai.ac.jp

Y. Li, G. Matsumura, S. Honda

Department of Physics and Electronics, Osaka Metropolitan University, Sakai, Osaka 599-8531 Japan

Stretchable devices, e-skin, machine learnings, action recognitions

Abstract:

Monitoring tactile pressure and recognizing action are important functionalities for artificial electronic skin (e-skin). Furthermore, in order to create conformable coverings for three-dimensional objects, an e-skin needs to be stretchable, without sacrificing sensitivity to tactile pressure. However, stretching of sensors normally affects their output stability. In this study, we develop a stretchable e-skin using laser-induced graphene and a liquid metal alloy, GaInSn, in an elastic ecoflex polymer to create a stretchable, resistive-type tactile pressure sensor. Furthermore, a pressure sensor array is fabricated as an e-skin, and output is signal-processed using machine learning. With this system, the e-skin also monitors its stretching state, with the result that tactile pressure can be calculated regardless of the degree of stretching. With machine learning-assisted e-skin, actions such as patting, sliding, and grabbing are successfully recognized in the manner of human skin.

Introduction

Electronic skin (e-skin) [1-5] that could measure pressure, temperature, and other stimuli like human skin, but with greater functionality, would allow diverse applications in robotics [6-7], wearable devices [8-10], and environmental monitoring [11] due to its mechanical flexibility. Mechanical flexibility is often achieved by selecting elastomer- or hydrogel-based materials as substrates and active materials for functionality to sense various stimuli [12]. By attaching a flexible e-skin to an object like a tape, large amounts of data can be obtained from non-planar surfaces, which conventional, rigid, Si-based sensors cannot do. Multi-functional flexible sensors to detect pressure, temperature, chemical substances, and electrical signals from muscle have been reported [6]. An alternative approach is to fabricate highly stable, high-performance bioresorbable sensors by integrating a microelectromechanical system device into a flexible film[8]. Surface-enhanced Raman spectroscopy has been used to detect molecules such as proteins[13-15]. However, such sensors cannot be applied to three-dimensional curved surfaces, limiting their applications, because most objects have non-planar structures. To address this issue, stretchable e-skins have been widely studied using elastomer substrates[16-19]. Stretchable tactile pressure sensors are especially attractive, since human skin has great sensitivity to tactile pressure, as well as stretchability. A variety of stretchable, conductive materials and structures have been proposed and demonstrated for potential e-skin devices[20-31]. Most such sensors have relied on resistive[21-22, 24, 27-29], capacitive[20, 26], and/or piezoelectric[23, 25] mechanisms. Furthermore, using flexible and/or stretchable e-skins, human computer interactions have already been employed in practical applications[32-34].

For stretchable tactile pressure sensors, other important factors include mechanical robustness and scalability. To maintain pressure detection functionality even under significant stretching, micro- and/or nano-conductive materials embedded in an elastomer substrate or liquid-phase materials are promising, because they can deform without cracks. In terms of mechanical robustness, liquid metals such as GaInSn and GaIn are of interest due to their high deformability[35]. However, conductance of the sensing layer needs to be lower than conductance of the electrodes, which requires a large sensor area because of the high conductivity of liquid metal. To achieve scalability, nano-carbon materials are good candidates due to their low-cost, macroscale formation, and low conductivity, compared to metals. To form a highly stretchable conductive layer, three-dimensional filament structures are preferred in order

to maintain conductivity under stretching. To create such structures with carbon materials, elastomer mixed with carbon black (CB) conductive particles has been reported [27]. Such materials have the capacity to stretch about 100%. However, multiple fabrication processes and additional structural considerations are required for sensor array integration. Another technique is to use laser-induced graphene (LIG)[36-40] as a sensing material. LIG is formed as a porous structure on a polyimide (PI) film. To make stretchable sensors, LIG is often transferred onto elastomer films[40-41], a process that usually employs a solution-based elastomer precursor and curing process, such that porous LIG is embedded in the elastomer. Because LIG can be patterned using a laser, it is easy to pattern sensors for integrated sensor arrays. After transfer, the three-dimensional stretchable conductive layer can be patterned in an elastomer. Using this unique structure of LIG in an elastomer, macroscale, low-cost, stretchable tactile pressure sensors can be created. Furthermore, because the conductance of LIG is much lower than that of typical electrode materials, the sensor can be readily designed and integrated with electrodes. However, to the best of our knowledge, an integrated LIG-based stretchable tactile pressure sensor array as an e-skin has yet to be achieved.

Although sensors reported have unique characteristics, such as high sensitivity, short response time, and/or low-power consumption [20-31], their outputs are often altered by stretching. By stretching a sensor, the electrical path becomes longer and the dielectric layer becomes thinner for resistive- and capacitive-type sensors, respectively, with the result that resistance and capacitance both increase. Piezoelectric sensors generate output voltage and current under stretching strain. For these reasons, it is hard to distinguish sensed stimuli from stretching. Although this challenge remains to be addressed in practical applications, classification of signals from sensors under stretching has rarely been discussed.

To address this problem and to develop highly scalable and stretchable e-skin harnessing the unique properties of LIG, here we demonstrate a wireless, stretchable e-skin to monitor tactile pressure and finger actions under both non-stretching and stretching conditions. For a systematic study of pressure sensitivity by imitating a sensor over curved surfaces, a balloon structure with a tactile pressure sensor array is demonstrated, and it is inflated by pumping air into the structure (Figure 1a-b). This allows us to characterize different stretching conditions by controlling the air volume. Furthermore, as proof-of-concept, pressure mapping has been demonstrated with/without inflation of the balloon. For more

practical uses of this sensor array, recognition of different actions such as patting, sliding, and grabbing was achieved using reservoir computing, a type of machine learning method. This recognition is accomplished by fabricating a tactile pressure sensor array and pressure distribution analyses, using machine learning. This shows the potential of this stretchable tactile pressure sensor array in human-computer interaction and e-skin.

To create a highly stretchable tactile pressure sensor, LIG[39-40] was used as the sensing material and a liquid metal, GaInSn (Galinstan), was used for electrodes. These were patterned on an ecoflex film, covered with another layer of ecoflex to protect the sensor from scratching. Figures 1c-f display a pixel of a tactile pressure, sensor array under inflation, and surface morphologies of LIG before and after transferring LIG into ecoflex observed by scanning electron microscope (SEM). More details about the fabrication process are provided in the Methods and in Figure S1.

Results and Discussion

LIG characterization

The stretchable sensing material was first analyzed by Raman spectroscopy (Figure S2). LIG was formed by scanning a PI film with a CO_2 laser, thereby carbonizing the PI surface [36-37]. The carbonized layer on the PI film has clear 2D and G peaks. In addtion to these peaks, D peaks, corresponding to defects in graphene, appeared. As a result, the LIG formed defective, multi-layered graphene, consistent with other reports [36-37, 39-40]. The effect of laser power was also studied. LIG quality was similar regardless of laser power (Figure S2). However, when laser power increases, the thickness of LIG on PI increases (Figure S3), because more PI film is converted into LIG. After transferring LIG into ecoflex film, the 2D peak disappeared while G and D peaks broadened, indicating that the transferred layer was non-crystalline carbon. This material change agrees well with previous reports [40]. This mechanism of crystallinity change after transfer is not understood, and needs to be addressed in a microstructural analysis of LIG. Although the crystallinity changed, the conductive LIG layer in the ecoflex is useful for sensor applications. One advantange to LIG is scalability, by virtue of using a laser to form it *in situ*. Even at lab fabrication level, relatively large (148 × 210 mm^2) patterning arrays can be formed (Figure

S4a-b). The uniformity of LIG was characterized by measuring the sheet resistance, which was 3.55±0.75 kΩ/sqr after transfer, whereas it was 45.3±2.1 Ω/sqr before (Figure S4c-d). The material became less uniform after transfer, most likely because of damage to LIG or a crystallinity change during transfer. However, this uniformity is acceptable, provided that sensors are calibrated.

Stretchable electrodes

Electrode materials are expected to have good electrical conductivity and stretchability without affecting sensor output. To suppress the effect of electrode resistance changes under stretching conditions, sensor design and materials to control resistance values are important. Sensor resistance should be much higher than that of electrodes. To meet these requirements, LIG and GaInSn were chosen as sensor and electrode materials, respectively. The resistance of LIG is much higher than that of GaInSn, even under tensile strain. To confirm this, first, a bending test of GaInSn in ecoflex was conducted to measure the resistance change as a function of bending radius. Because GaInSn was formed around a strain-neutral region of the ecoflex film under bending, the resistance change of the GaInSn electrode is small (Figure S5a). Importantly, GaInSn resistance (< 2 Ω, depending on the design) is much lower than that of the LIG strain sensor (~7 kΩ). Next, GaInSn was stretched up to 100 %. Since the resistance is given by $\rho L/S$, where ρ is the resistivity, L is the length, and S is the cross-sectional area of the electrode, resistance increases under stretching due to longer L and smaller S. In fact, when the electrode was stretched to 100%, the resistance increased from ~2 Ω to ~22 Ω (Figure S5b). Although the resistance of the GaInSn electrode increases significantly under stretching, this change of about 20 Ω is negligible compared to the resistance of the LIG strain sensor (~7 kΩ). In regard to durability, cycle tests applying strain to the GaInSn electrode were conducted. While the resistance change ratio under application of pressure (~102 kPa) shows some change at the beginning of the test, the resistance change is still small enough (Figure S5c). Furthermore, the electrode was stable even under stretching of 25 % for as many as 10,000 cycles with little fluctuation < ~0.2 Ω (Figure S5d).

Tactile pressure sensor

Tactile pressure sensors comprising LIG as the sensor and GaInSn in ecoflex as the electrode were then characterized. The mechanism for sensing pressure over LIG is to monitor resistance changes caused by deformation of LIG under applied pressure (Figure 2a). Under pressure, LIG resistance increases due to squeezing, and this resistance change can be used to calculate the applied pressure. To understand the effect of laser power for sensor characterization, laser power was changed from 10 W to 20 W. Based on results from Raman spectroscopy, the quality of amorphous carbon and of LIG remained almost unchanged. However, the LIG layer formed at higher laser power is thicker than that at lower laser power (Figure S3). 10-W laser power used to form LIG achieves the highest sensitivity to pressure, most likely because the low density of graphene corresponding to thinner LIG in ecoflex reduces the probability of making electrical contact between graphene flakes in ecoflex under strain (Figure 2b). First, the resistance change ratio, $\Delta R/R_0$, where ΔR is the difference between initial resistance (R_0) and resistance under applied pressure, was measured as a function of applied pressure up to 140 kPa (Figure 2c). There were two trends at low and high pressure. At pressure less than 80 kPa, sensitivity of the sensor is 2.73%/kPa extracted by linear fitting. From 80 to140 kPa, its sensitivity is 10.49 %/kPa. This sensitivity difference between low and high pressure is most likely due to structural deformation differences. At low pressure, an object depresses the surface of ecoflex by 1.5 mm at 39 kPa, whereas a deformation of 3.3 mm occurred at high-pressure (123 kPa) (Figure 2c). Because the top ecoflex layer is 2.5 mm thick, high pressure probably affects both the top and bottom ecoflex layers, including mostly the LIG sensor layer, resulting in sensitivity increases at high pressure.

Real-time pressure-sensor outputs and hysteresis show that the sensor has relatively stable operation during application and release of pressure (Figure 2d-e). To explore pressure response times and repeatability, cycle tests, applying and releasing pressure, were conducted. The response time was relatively fast (~70 ms) (Figure 2f). However, recovery was much longer, at about 2.6 s. This slow recovery reflects the capacity of the elastomer (ecoflex) with LIG to recover its initial state. By applying surface texturing of LIG/Ecoflex using laser scanning to roughen the surface, recovery speed was improved to 1.3 s (Figure S6). However, this is still a preliminary result, and the reason for the enhancement of the response cannot be identified with certainty. Because of this preliminary result

regarding LIG/ecoflex with texturization, this study used LIG/ecoflex without texturization for all tests. For repeatability, output resistance remains almost consistent during 10,000 cycles over 12 h, although sensor resistance changes slightly at the beginning of the cycle test (Figure 2g).

Because an elastomer film was used for this tactile pressure sensor, sensor resistance also changes with temperature, due to the relatively large thermal expansion of ecoflex. To confirm the effect of temperature on the tactile pressure sensor, the resistance change was measured at different temperatures. As expected, resistance increased by 50% when the temperature increased from 28.8 ºC to 80 ºC, which was most likely caused by thermal expansion of ecoflex (Figure S7a). Although resistance changed with temperature, pressure sensitivity extracted from the resistance change ratio as a function of pressure at different temperatures (30 ºC and 70 ºC) remained almost the same (Figure S7b). For this comparison, initial resistance, R_0, was set separately at each temperature. This suggests that pressure can be readily calculated with a constant sensitivity parameter, even though temperature monitoring is required to calibrate the pressure.

Next, chemical stability was tested by exposing the sensor to moisture changes and different solutions. To change the moisture level, a temperature and humidity controllable environmental oven was used. The temperature was set at 28.9 ºC and humidity was changed from 40% to 80% (Figure S8). Although there was a small drift of sensor output over time, no resistance change was caused by the humidity change. Sensor responses to solutions with different pHs over the sensor were then measured, resulting in negligible change of sensor outputs regardless of pH (Figure S9a-c). Furthermore, NaCl solution to imitate sweat was applied to the sensor. As in pH tests, output did not change even at an NaCl concentration of 40 mmol/L (Figure S9d). This stability is possible because the sensor is sandwiched in ecoflex, which served as a protective layer.

To achieve tactile pressure monitoring even under stretching, sensor responses under stretching were investigated. Due to the highly stretchable ecoflex film with porous LIG and GaInSn electrodes, the sensor functions during stretching of over 200% (Figure 3a and S10). Due to structural deformation, sensor resistance increases to ~400% from the initial state to 200% stretching. Sensor output continues without breaking the electrical connection even under 200% stretching. As a control, CB, which is the same carbon-based material as LIG in the ecoflex film, was tested as a stretchable sensor. While tactile

pressure could be measured (Figure S11a), the sensor was electrically disconnected at stretching exceeding 7% (Figure S11b), demonstrating that the CB sensor cannot be used for a stretchable e-skin, as is possible with porous LIG in ecoflex. Furthermore, the pressure sensor can stably detect pressure under 20% stretching (Figure 3b). Importantly, the pressure sensor sensitivity is ~4 %/kPa, and it does not change significantly with stretching (Figure 3c and S12). However, the sensitivity tends to decrease slightly at higher stretches. This may be due to lower density of LIG in ecoflex under higher stretching conditions, resulting in lower contact probability between LIGs under applied pressure. For reliability of sensor output, cycle tests of pressure application under stretching were conducted (Figure 3d). The sensor was stretched to 20% and 6.25 kPa pressure was applied. In the beginning, sensor resistance increased about 8%, and then, without pressure application, the base resistance gradually decreased to 3% above its initial value, after which it stabilized. In this experiment, 700 cycles were tested, and the results show relatively stable operation of pressure monitoring under stretching. Thus, we conclude that this pressure sensor design can be used for both non-stretching and stretching conditions with minimal calibration of output resistance under stretching. However, due to the initial resistance difference during stretching, some signal processing to recognize the condition is required, as discussed below.

With confirmation of acceptable, stable operation even under stretching, a balloon-type 4×4 tactile pressure sensor array was fabricated (Figure 3e). To inflate the sensor array with compressed air, another ecoflex film was attached under the pressure sensor array film, and the edges of the films were bonded using ecoflex solution. After curing the solution, a balloon-type e-skin was achieved. By injecting air into the balloon, inflation was controlled (Figure 3f). This inflated e-skin can be formed like a three-dimensional robotic finger or hand for example. Depending on the amount of inflation, corresponding to the air volume in the e-skin, resistance change ratios were characterized by applying pressure over the sensor (Figure 3g). The results show that the resistance change ratio, i.e., the sensitivity, increased under air volumes <80 mL from a flat state, i.e., air volume = 0 mL. However, by increasing the air volume up to 120 mL, sensitivity returned to its original value before inflation. On the other hand, as discussed in Figure 3c, sensitivity is almost constant under unidirectional stretch in the range between 0 and 20 %. This phenomenon shown in Figure 3g is most likely due to symmetric stretching of LIG, where the strain distribution of LIG is more complex compared to the unidirectional stretch. As a result,

depending on strain amplitude caused by inflation, the density of porous LIG changes, resulting in higher and lower sensitivity. Because of this, LIG density is important to control sensitivity. However, confirmation will require more microscopic analyses of LIG density changes, and that is beyond the scope of this study.

The advantage of the elastomer body of the sensor is that it resists damage from sharp objects. Since ecoflex film is hard to cut, even using a knife, the sensor is protected in various applications, including robotic hands. Even if the ecoflex sustains damage and LIG is partially severed, due to the strong recovery property of ecoflex, it can be still used as a pressure sensor (Figure S13). After damage of the LIG region with a knife, the pressure sensor response was maintained for as much as 8 weeks (Figure S13b-c.)

With the inflated e-skin, pressure distribution was monitored by reading all pixels. A wireless system using a low-energy Bluetooth (BLE) module to record 16 sensor outputs was developed (Figure S14). Recorded data were transmitted to a laptop computer. For a preliminary demonstration of the feasibility of wireless e-skin, clip-type electrical wirings between the e-skin and wireless system were used. Before inflation, locations of objects were mapped (Figure 4a-c), and after inflation with 80 mL air, pressure mapping was successfully monitored (Figure 4d-g and movie S1).

The yield was calculated based on the number of successful sensor formations in stretchable e-skin. The yield in this study was ~94%. However, as discussed in Figure S4, since there is resistance variation in fabricated LIG arrays, sensor calibration is required.

Machine learning-assisted action recognition

Action recognition by the e-skin, based on pressure distribution under motion, was implemented using machine learning. In order to classify patting, sliding, and grabbing actions, (termed “output1”) while the sensor array was in flat and inflated states, an echo state network (ESN), which is the most popular reservoir computing framework, was introduced[42-45]. With the ESN, it was possible to achieve accurate classification with a small number of data points, resulting in short training times. These characteristics will be beneficial to increase the number of actions that can be classified in the future. An original ESN algorithm was developed for this application (Figure 5a).

To classify the three actions, different values for all 16 sensor outputs were chosen as inputs to the ESN. By taking differential values for sensor outputs, it was possible to ignore initial sensor values necessitated by sensor-to-sensor variation. This enabled us to identify changing sensor outputs for patting, sliding, and grabbing, and helped ESN to learn easily. These three actions have different time ranges from a stable state to a moving state and from a moving state to a stable state. For this time difference, the leaking rate, was introduced to the ESN to accurately distinguish between these actions.

Flat or inflated states, termed "Output2", were calculated by logistic regression directly from the sensor output. After optimizing the hyper-parameters and algorithm, predicted results of sensor outputs (upper), output1 (middle), and output2 (bottom) in flat and inflated states were analyzed (Figure 5b-c). To evaluate output1 and output2, Leave-One-Out Cross Validation (LOOCV) was used. Ten datasets (5 in a flat state, and 5 in an inflated state) were prepared. One dataset was used as test data and the others were used as training data. After recognition accuracy was calculated, test data were exchanged until all datasets had been used as test data. When calculating accuracy of "output1", the macro-f1 score was introduced because numbers of patting, sliding, and grabbing states were different. "Output2" was evaluated with the accuracy score. Figure S15 shows grid search results of "output1" when one dataset was used as test data and the others were employed as training data to define optimized hyper-parameters. The reason for separating two analytical processes as "output1" and "output2" was the accuracy difference between the two (Table S1). For "output1" prediction, a differential is better than a raw value, whereas a raw value is better for "output2" than a differential. When results with and without ESN were compared, introducing ESN increased accuracy for both "output1" and "output2." However, the result of "output2" with ESN when input was raw data, was almost same as the result without ESN. To simplify the system, we decided to use it without ESN for output2. By applying two analytical processes, both output1 and output2 with high accuracy were achieved. After compiling all results, confusion matrices of output1 (Figure 5d) and output2 (Figure 5e) are displayed. The e-skin can recognize actions and stretched states simultaneouly from sensor output. Because prediction of a stretching state can be estimated using ESN, tactile pressure can be calculated based on the sensitivity and stretching rate, which until now, has been the challenge for stretchable e-skin to distinguish tactile pressure and stretch. Using prediction outputs, continuous animation was demonstrated as a proof-of-concept for wireless

stretchable e-skin system (Figure 5f). It was confirmed that ESN outputs and animation followed real actions over e-skin. These results prove that the stretchable e-skin can recognize each action with relatively high accuracy, regardless of being in a flat or stretched state.

Based on these characteristics, a comparison of stretchable pressure sensors from various pioneering studies is summarized in Table S2. Different materials have different advantages; however, most studies have not examined sensor functionalities under stretching or scratching damage to the sensors, which we examined systematically in this study. Furthermore, the e-skin reported in this study has similar or better performance than those of other sensors, and it can recognize action regardless of stretching conditions

Conclusion

In summary, by optimizing and designing both structure and materials, a stretchable pressure-sensitive e-skin demonstrated good durability, even under stretching. The pressure sensor exhibits stable resistance change and small hysteresis to applied pressure, with high stability for at least 10,000 cycles. Furthermore, the pressure sensor can be stretched more than 200% while maintaining a stable resistance change and sensitivity. e-skins may be damaged by sharp objects. To protect against this, a relatively thick ecoflex elastic polymer was chosen. In addition, due to the elastic nature of ecoflex, even if LIG of a sensor was partially cut, the sensor maintained stable output for at least eight weeks after the damage. Finally, as a proof-of-concept, an e-skin was demonstrated with and without inflation, and an action recognition system using machine learning was developed. In both flat and inflated states, tactile pressure mapping was correctly detected. More importantly, based on the mapping results in time, patting, sliding, and grabbing were successfully recognized with relatively high accuracy, like human skin, using the developed ESN and logistic regression algorithm. For practical application as an e-skin, device cost is important, and GaInSn, in particular, is relatively expensive (roughly US$3/g and ~7 g is used for the e-skin demonstrated in this study). However, it may be possible to reduce the device cost by using less GaInSn to make narrower and thinner patterns for the electrodes since the conductivity is

much higher than that of LIG. We believe that this achievement will facilitate development of human-machine-computer interactions and e-skin.

Experimental Section/Methods

Fabrication process: Figure S1 shows fabrication of this pressure sensor. First, a mold was fabricated using a 3-D printer, and ecoflex solution was poured onto this mold and cured in an environmental oven at 90 ºC. This created channels for liquid GaInSn alloy. LIG was formed on a PI film by exposing it to a laser. Due to the thermal effect of the laser over PI, PI was carbonized, resulting in multi-layer, defective graphene[39-40]. The ecoflex solution was poured over the LIG/PI film, and LIG was transferred to the ecoflex film after curing it for 15 min in an environmental oven. These two ecoflex films were bonded using ecoflex solution. After lamination, GaInSn was injected into the channels to form the electrodes. Finally, the injection ports were sealed with ecoflex solution to complete sensor fabrication.

Supporting Information

Supporting Information is available from the Wiley Online Library or from the author.

Acknowledgements

This work was partially supported by JST AIP Accelerated Program (No. JPMJCR21U1), JSPS KAKENHI (Grant No. JP22H00594), the Murata Science Foundation, the Hitachi Global Foundation, and the Takeda Science Foundation.

Conflict of Interest

The authors declare no conflict of interest.

Data Availability Statement

The data that support the findings of this study are available from the corresponding author upon reasonable request.

Received: ((will be filled in by the editorial staff))

Revised: ((will be filled in by the editorial staff))

Published online: ((will be filled in by the editorial staff))

References

[1] T. Someya, T. Sekitani, S. Iba, Y. Kato, H. Kawaguchi, T. Sakurai, *Proc. Natl. Acad. Sci. U.S.A.* **2004**, 101, 9966.

[2] T. Someya, Y. Kato, T. Sekitani, S. Iba, Y. Noguchi, Y. Murase, H. Kawaguchi, T. Sakurai, *Proc. Natl. Acad. Sci. U.S.A.* **2005**, 102, 12321.

[3] D. H. Kim, N. Lu, R. Ma, Y. S. Kim, R. H. Kim, S. Wang, J. Wu, S. M. Won, H. Tao, A. Islam, K. J. Yu, T. I. Kim, R. Chowdhury, M. Ying, L. Xu, M. Li, H. J. Chung, H. Keum, M. McCormick, P. Liu, Y. W. Zhang, F. G. Omenetto, Y. Huang, T. Coleman, J. A. Rogers, *Science* **2011**, 333, 838.

[4] G. Schwartz, B. C. Tee, J. Mei, A. L. Appleton, H. Kim do, H. Wang, Z. Bao, *Nat. Commun.* **2013**, 4, 1859.

[5] K. Takei, T. Takahashi, J. C. Ho, H. Ko, A. G. Gillies, P. W. Leu, R. S. Fearing, A. Javey, *Nat. Mater.* **2010**, 9, 821.

[6] Y. Yu, J. Li, S. A. Solomon, J. Min, J. Tu, W. Guo, C. Xu, Y. Song, W. Gao, *Sci. Robot.* **2022**, 7, eabn0495.

[7] T. Yamaguchi, T. Kashiwagi, T. Arie, S. Akita, K. Takei, *Adv. Intell. Syst.* **2019**, 1, 1900018.

[8] Q. Yang, T.-L. Liu, Y. Xue, H. Wang, Y. Xu, B. Emon, M. Wu, C. Rountree, T. Wei, I. Kandela, C. R. Haney, A. Brikha, I. Stepien, J. Hornick, R. A. Sponenburg, C. Cheng, L. Ladehoff, Y. Chen, Z. Hu, C. Wu, M. Han, J. M. Torkelson, Y. Kozorovitskiy, M. T. A. Saif, Y. Huang, J.-K. Chang, J. A. Rogers, *Nat. Electron.* **2022**, 5, 526.

[9] Y. Yang, Y. Song, X. Bo, J. Min, O. S. Pak, L. Zhu, M. Wang, J. Tu, A. Kogan, H. Zhang, T. K. Hsiai, Z. Li, W. Gao, *Nat. Biotech.* **2019**, 38, 217.

[10] S. S. Kwak, S. Yoo, R. Avila, H. U. Chung, H. Jeong, C. Liu, J. L. Vogl, J. Kim, H. J. Yoon, Y. Park, H. Ryu, G. Lee, J. Kim, J. Koo, Y. S. Oh, S. Kim, S. Xu, Z. Zhao, Z. Xie, Y. Huang, J. A. Rogers, *Adv. Mater.* **2021**, e2103974.

[11] Y. Lu, K. Xu, L. Zhang, M. Deguchi, H. Shishido, T. Arie, R. Pan, A. Hayashi, L. Shen, S. Akita, K. Takei, *ACS Nano* **2020**, 14, 10966.

[12] M. A. Zahed, M. Sharifuzzaman, H. Yoon, M. Asaduzzaman, D. K. Kim, S. Jeong, G. B. Pradhan, Y. D. Shin, S. H. Yoon, S. Sharma, S. Zhang, J. Y. Park, *Adv. Funct. Mater.* **2022**, 32, 2208344.

[13] Y.-J. Yeh, C.-J. Cho, J.-S. Benas, K.-L. Tung, C.-C. Kuo, W.-H. Chiang, *ACS Appl. Nano Mater.* **2023**, 6, 10115.

[14] Y. J. Yeh, T. N. Le, W. W. Hsiao, K. L. Tung, K. K. Ostrikov, W. H. Chiang, *Anal. Chim. Acta* **2023**, 1239, 340651.

[15] K. Xu, R. Zhou, K. Takei, M. Hong, *Adv. Sci.* **2019**, 6, 1900925.

[16] Z. Liu, Y. Zheng, L. Jin, K. Chen, H. Zhai, Q. Huang, Z. Chen, Y. Yi, M. Umar, L. Xu, G. Li, Q. Song, P. Yue, Y. Li, Z. Zheng, *Adv. Funct. Mater.* **2021**, 31, 2007622.

[17] J. W. Lee, R. Xu, S. Lee, K. I. Jang, Y. Yang, A. Banks, K. J. Yu, J. Kim, S. Xu, S. Ma, S. W. Jang, P. Won, Y. Li, B. H. Kim, J. Y. Choe, S. Huh, Y. H. Kwon, Y. Huang, U. Paik, J. A. Rogers, *Proc.*

Natl. Acad. Sci. U.S.A. **2016**, 113, 6131.

[18] S. Wang, J. Xu, W. Wang, G. N. Wang, R. Rastak, F. Molina-Lopez, J. W. Chung, S. Niu, V. R. Feig, J. Lopez, T. Lei, S. K. Kwon, Y. Kim, A. M. Foudeh, A. Ehrlich, A. Gasperini, Y. Yun, B. Murmann, J. B. Tok, Z. Bao, *Nature* **2018**, 555, 83.

[19] H. Choi, Y. Luo, G. Olson, P. Won, J. H. Shin, J. Ok, Y. J. Yang, T. i. Kim, C. Majidi, *Adv. Funct. Mater.* **2023**, 33, 2301388.

[20] Q. Su, Q. Zhou, Y. Li, Y. Chen, S.-Y. Teng, J. T. Kelleher, R. Nith, P. Cheng, N. Li, W. Liu, S. Dai, Y. Liu, A. Mazursky, J. Xu, L. Jin, P. Lopes, S. Wang, *Sci. Adv.* **2021**, 7, eabi4563.

[21] Y. Zhang, S. Liu, Y. Miao, H. Yang, X. Chen, X. Xiao, Z. Jiang, X. Chen, B. Nie, J. Liu, *ACS Appl. Mater. Interfaces* **2020**, 12, 27961.

[22] W. Wang, Y. Jiang, D. Zhong, Z. Zhang, S. Choudhury, J.-C. Lai, H. Gong, S. Niu, X. Yan, Y. Zheng, C.-C. Shih, R. Ning, Q. Lin, D. Li, Y.-H. Kim, J. Kim, Y.-X. Wang, C. Zhao, C. Xu, X. Ji, Y. Nishio, H. Lyu, J. B.-H. Tok, Z. Bao, *Science* **2023**, 380, 735.

[23] Y. C. Lai, J. Deng, R. Liu, Y. C. Hsiao, S. L. Zhang, W. Peng, H. M. Wu, X. Wang, Z. L. Wang, *Adv. Mater.* **2018**, e1801114.

[24] R. Matsuda, S. Mizuguchi, F. Nakamura, T. Endo, Y. Isoda, G. Inamori, H. Ota, *Scientific reports* **2020**, 10, 12666.

[25] J. Yu, L. Chen, X. Hou, J. Mu, J. He, W. Geng, X. Qiao, X. Chou, *J. Materiomics* **2022**, 8, 247.

[26] Y. Zhang, J. Yang, X. Hou, G. Li, L. Wang, N. Bai, M. Cai, L. Zhao, Y. Wang, J. Zhang, K. Chen, X. Wu, C. Yang, Y. Dai, Z. Zhang, C. F. Guo, *Nat. Commun.* **2022**, 13, 1317.

[27] W. Kim, D. Kim, J. Kim, S. U. Park, H. K. Lee, J. Joo, S. G. Lee, J. W. Chae, J. Kim, S. Han, H. W. Baac, S. M. Won, *Adv. Mater. Technol.* **2023**, 8, 2300068.

[28] G. Wang, M. Wang, M. Zheng, B. Ebo, C. Xu, Z. Liu, L. He, *ACS Appl. Nano Mater.* **2023**, 6, 9865.

[29] Y. Zhang, Q. Lu, J. He, Z. Huo, R. Zhou, X. Han, M. Jia, C. Pan, Z. L. Wang, J. Zhai, *Nat. Commun.* **2023**, 14, 1252.

[30] X. Zhang, M. Wang, Y. Wu, X. Chen, Y. Wu, Q. Fu, H. Deng, *Adv. Funct. Mater.* **2022**, 33, 2210027.

[31] Z. Bai, X. Wang, M. Zheng, O. Yue, M. Huang, X. Zou, B. Cui, L. Xie, S. Dong, J. Shang, G. Gong, A. M. Blocki, J. Guo, X. Liu, *Adv. Funct. Mater.* **2023**, 33, 2212856.

[32] Z. Bai, T. He, Z. Zhang, Y. Xu, Z. Zhang, Q. Shi, Y. Yang, B. Zhou, M. Zhu, J. Guo, C. Lee, *Nano Energy* **2022**, 94.

[33] M. Chao, P. Di, Y. Yuan, Y. Xu, L. Zhang, P. Wan, *Nano Energy* **2023**, 108.

[34] G. Ye, Y. Wan, J. Wu, W. Zhuang, Z. Zhou, T. Jin, J. Zi, D. Zhang, X. Geng, P. Yang, *Nano Energy* **2022**, 97, 107148.

[35] Y. R. Jeong, J. Kim, Z. Xie, Y. Xue, S. M. Won, G. Lee, S. W. Jin, S. Y. Hong, X. Feng, Y. Huang, J. A. Rogers, J. S. Ha, *NPG Asia Materials* **2017**, 9.

[36] J. Lin, Z. Peng, Y. Liu, F. Ruiz-Zepeda, R. Ye, E. L. Samuel, M. J. Yacaman, B. I. Yakobson, J. M. Tour, *Nat. Commun.* **2014**, 5, 5714.

[37] R. Ye, D. K. James, J. M. Tour, *Acc. Chem. Res.* **2018**, 51, 1609.

[38] J. L. Beckham, J. T. Li, M. G. Stanford, W. Chen, E. A. McHugh, P. A. Advincula, K. M. Wyss, Y. Chyan, W. L. Boldman, P. D. Rack, J. M. Tour, *ACS Nano* **2021**, 15, 8976.

[39] K. Xu, Y. Fujita, Y. Lu, S. Honda, M. Shiomi, T. Arie, S. Akita, K. Takei, *Adv. Mater.* **2021**, 33, e2008701.

[40] S. Wakabayashi, T. Arie, S. Akita, K. Nakajima, K. Takei, *Adv. Mater.* **2022**, 34, 2201663.

[41] D. X. Luong, K. Yang, J. Yoon, S. P. Singh, T. Wang, C. J. Arnusch, J. M. Tour, *ACS Nano* **2019**, 13, 2579.

[42] K. Nakajima, I. Fischer, *Springer Nature* **2021**.

[43] M. Lukoševičius, H. Jaeger, *Comput. Sci. Rev.* **2009**, 3, 127.

[44] H. Jaeger, *GMD Report* **2002**, 152, 1.

[45] H. Jaeger, *Technical Report GMD Report* **2001**, 148, 1.

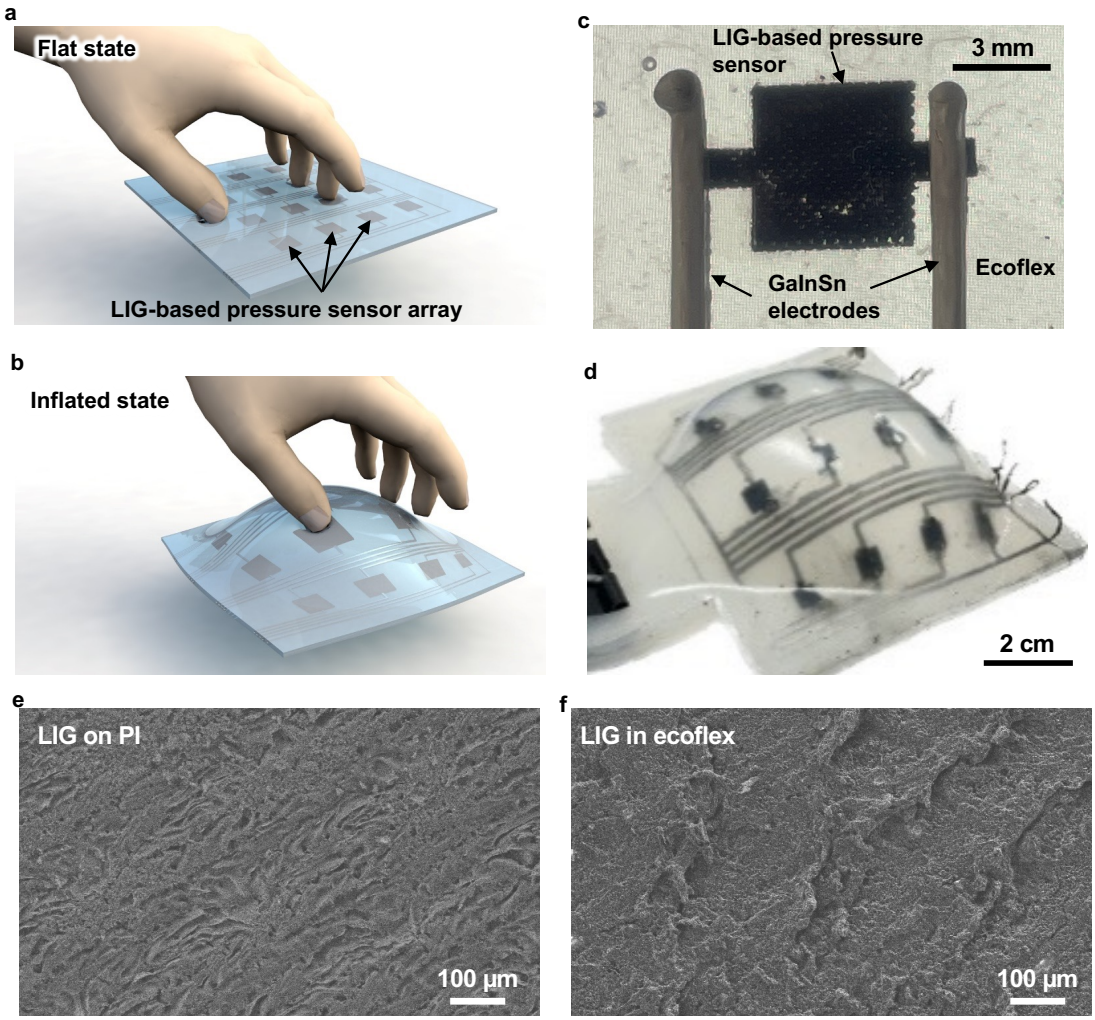

Figure 1. Schematic images of an inflatable e-skin (a) before (flat) and (b) after inflation. Photos of (c) a pressure sensor and (d) an inflated e-skin. Surface morphologies observed by SEM on (e) PI film and (f) ecoflex film.

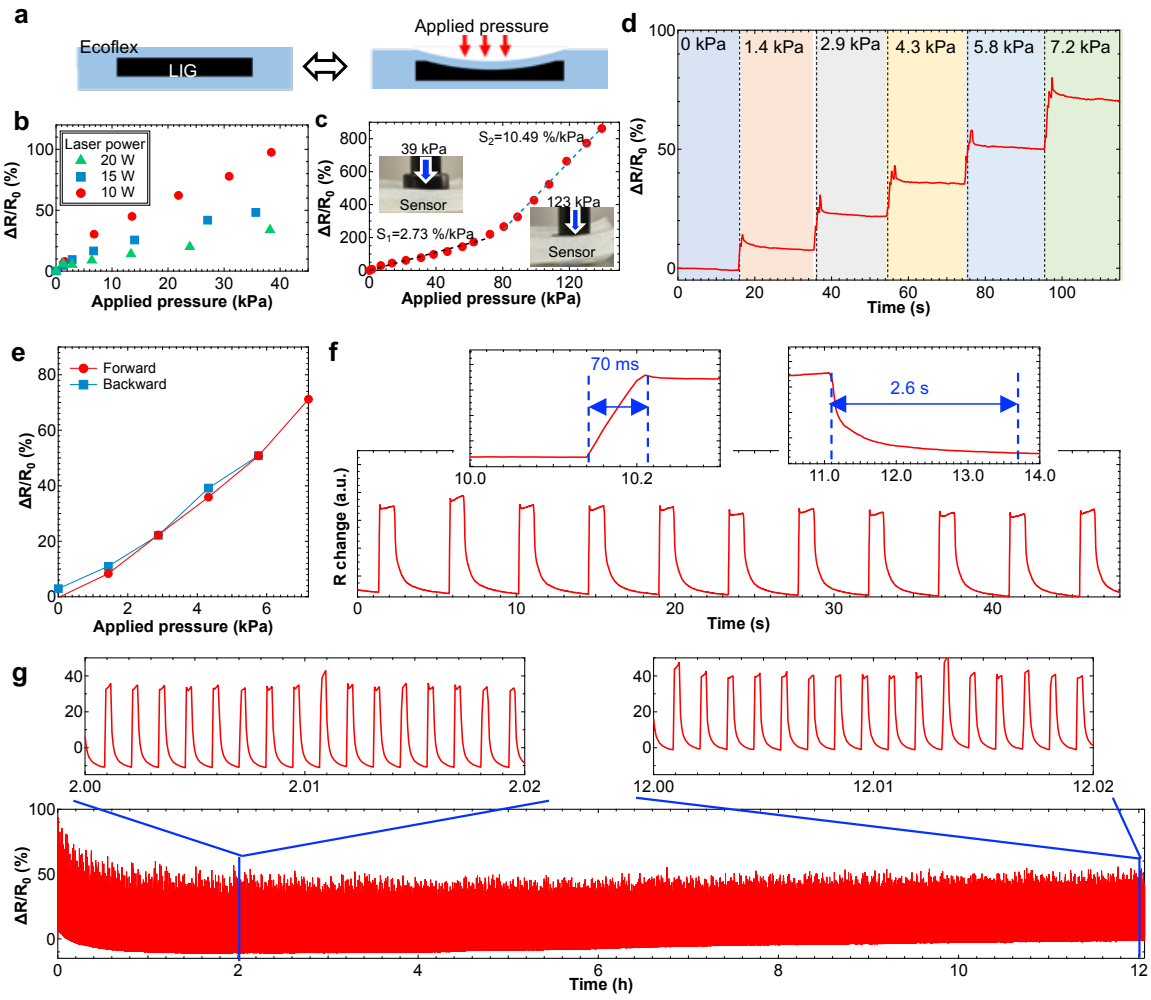

Figure 2. Electrical characteristics of the pressure sensor without inflation. (a) Pressure-sensing mechanism. (b) Resistance change ratio as a function of applied pressure at different laser powers during formation of LIG. (c) Resistance change ratio at low- and high-pressure. (d) Real-time resistance change at different applied pressures. (e) Hysteresis when pressure was applied and released. (f) Response-time monitoring of the sensor. (g) Cycle test of the pressure sensor for >10,000 cycles.

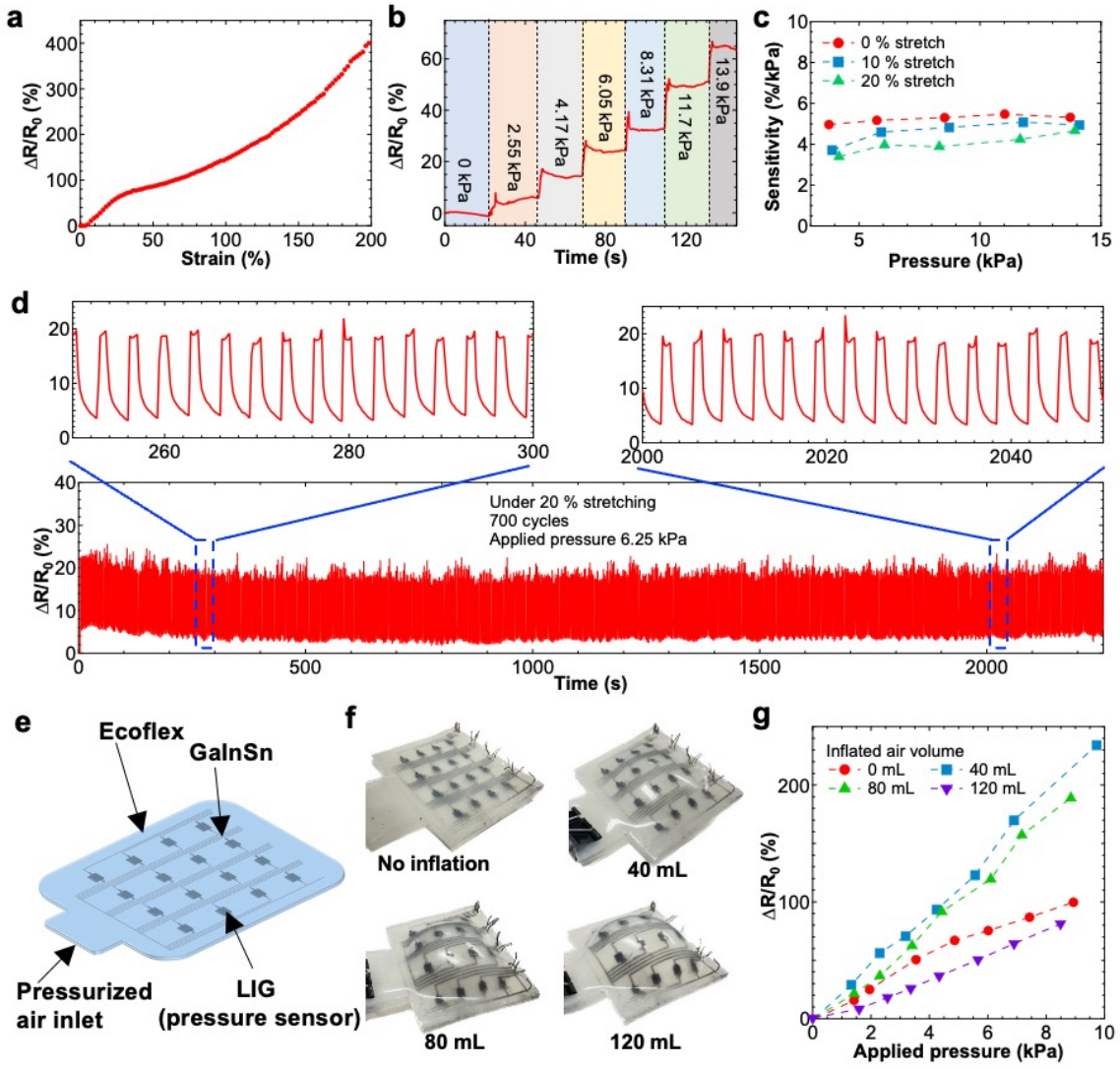

Figure 3. Pressure sensor characteristics during stretching or inflation. (a) Resistance change ratio as a function of tensile strain. (b) Real-time resistance change ratio at different applied pressures during 20% stretching of the sensor. (c) Pressure sensor sensitivity as a function of pressure under different stretching conditions. (d) Cycle test of the pressure sensor under 20% stretching up to 700 cycles. (e) Schematic of an inflated e-skin. (f) Photos of the e-skin before and during inflation at different air volumes. (g) Resistance change ratio as a function of applied pressure at different degrees of inflation.

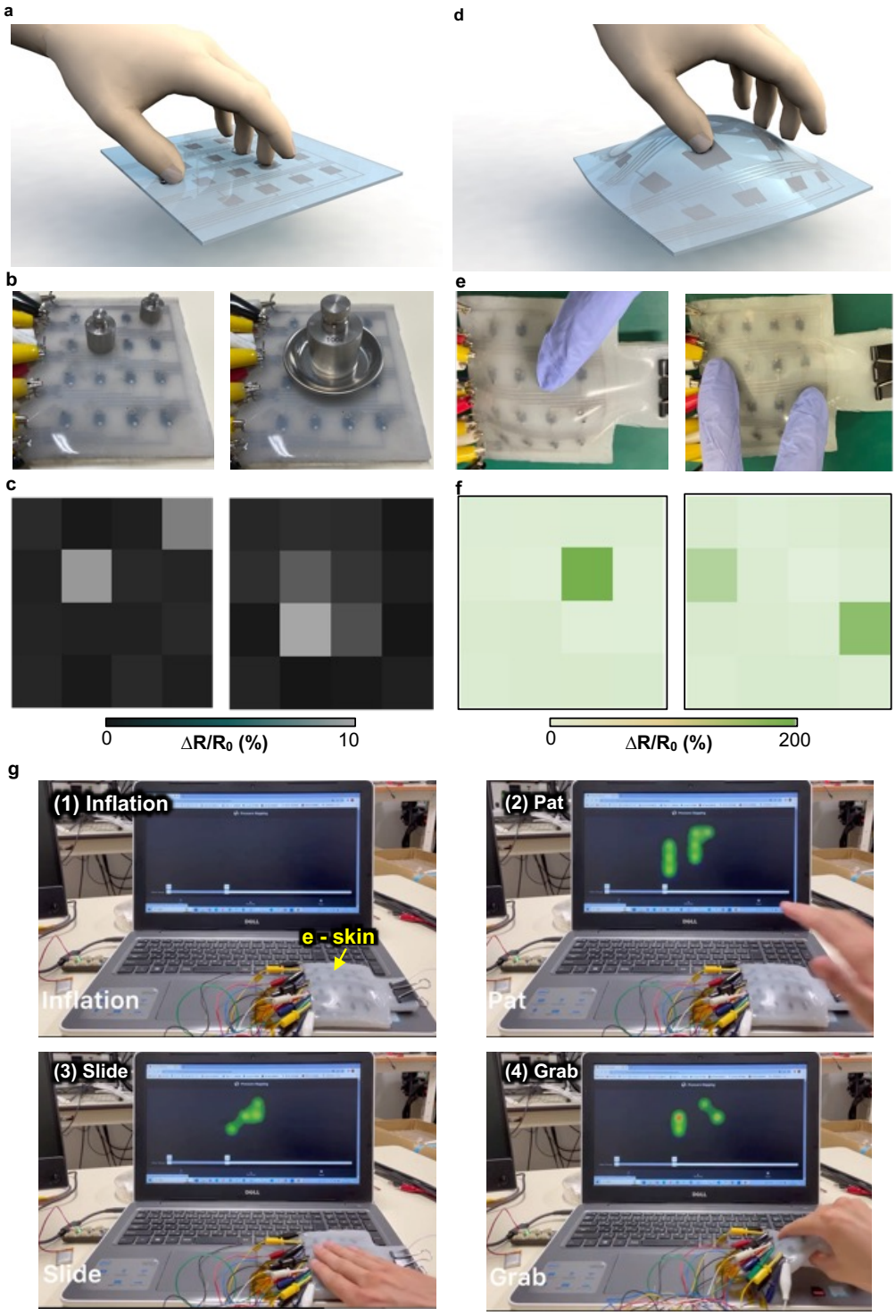

Figure 4. (a) Schematic, (b) photos, and (c) pressure distribution mapping of the e-skin without inflation. (d) Schematic, (e) photos, and (f) pressure distribution mapping of the e-skin after inflation with 80 mL of air. (g) Demonstration of the wireless e-skin under inflation.

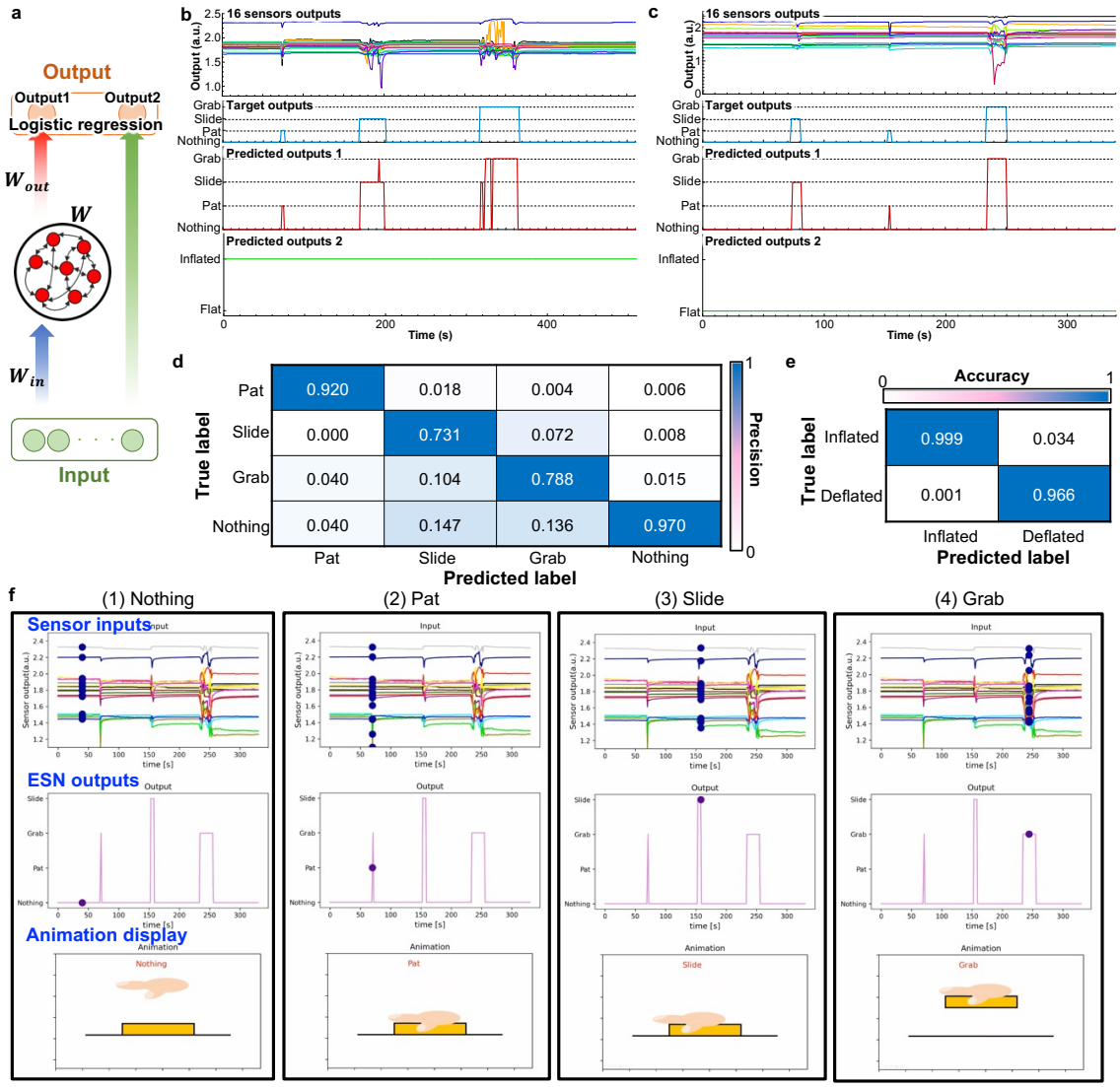

Figure 5. (a) Schematic algorithm of machine learning. Sensor outputs, target outputs, and prediction outputs for gestures and inflation (b) without inflation (flat state) and (c) with inflation. Confusion matrices of (d) actions and (e) inflation. (f) Demonstration of sensor inputs, ESN prediction outputs, and animation.

A stretchable tactile pressure sensor array with highly accurate tactile pressure detection is developed in both unstretched and stretched states as an electronic skin (e-skin). To achieve greater functionality, resembling that of human skin, action recognition over the e-skin is successfully demonstrated by analyzing pressure distribution and motions using an echo-state network regardless of the degree of stretching.

*Yanpeng Li, Guren Matsumura, Yan Xuan, Satoko Honda, Kuniharu Takei**

Stretchable electronic skin with an action recognition system

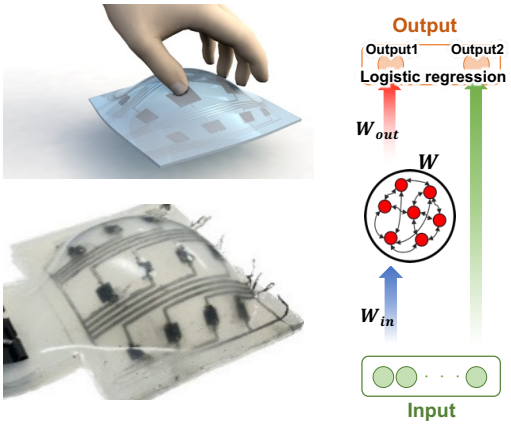

Supporting Information

Stretchable electronic skin with an action recognition system

*Yanpeng Li, Guren Matsumura, Yan Xuan, Satoko Honda, Kuniharu Takei**

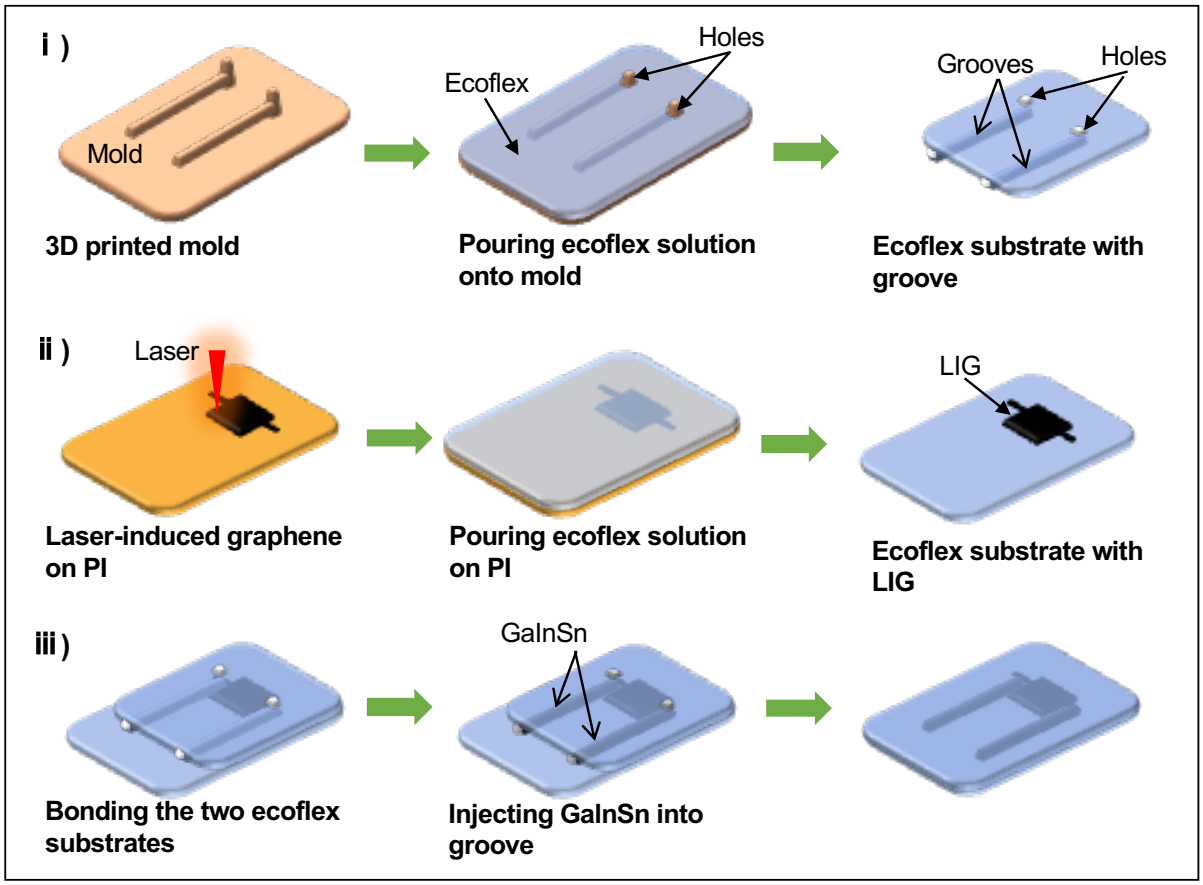

Figure S1. Schematic of the fabrication process.

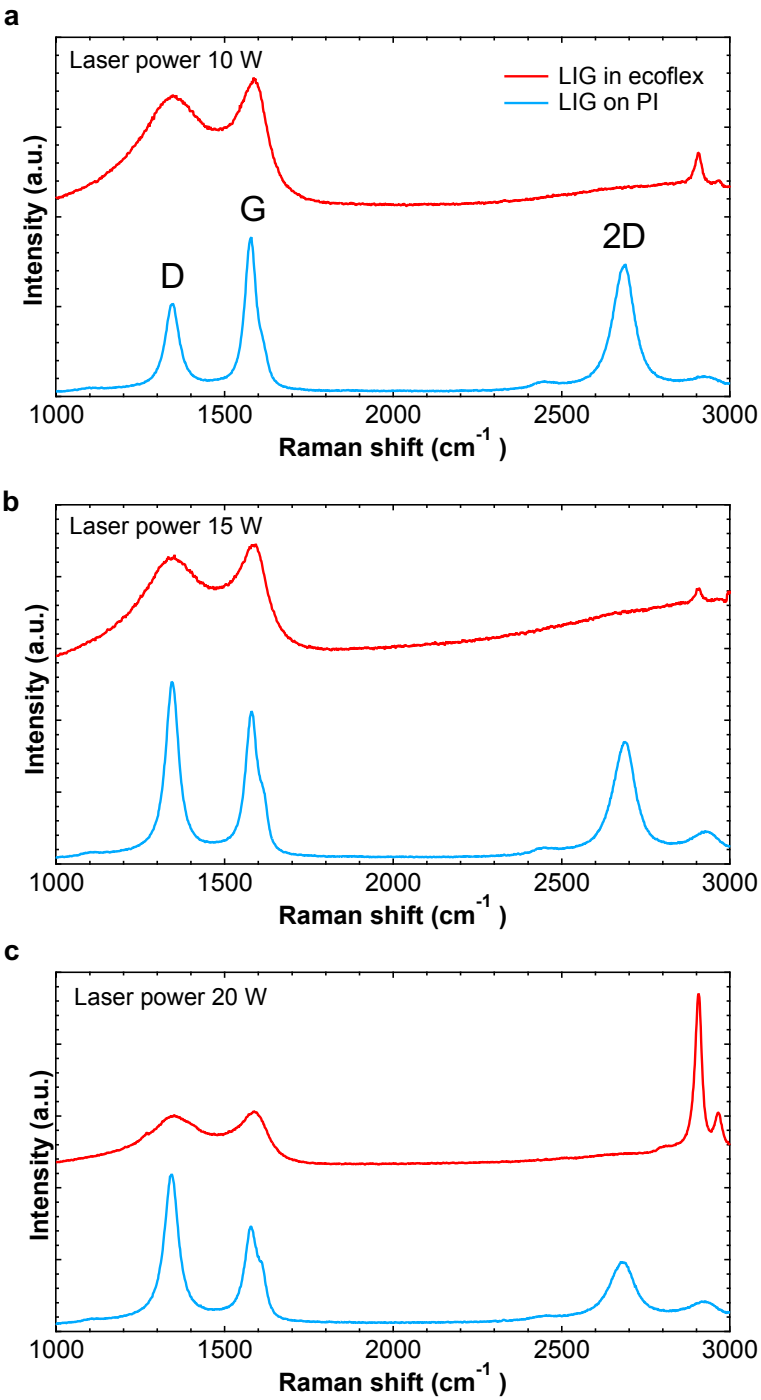

Figure S2. Raman spectroscopy of LIG on PI and in ecoflex formed by laser power at (a) 10 W, (b) 15 W, and (c) 20 W.

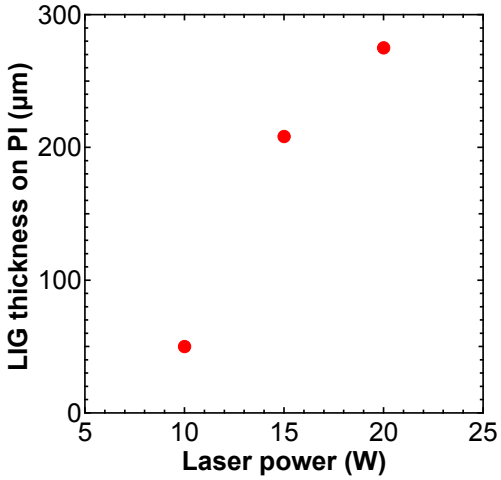

Figure S3. LIG thickness on the PI film formed at different laser powers.

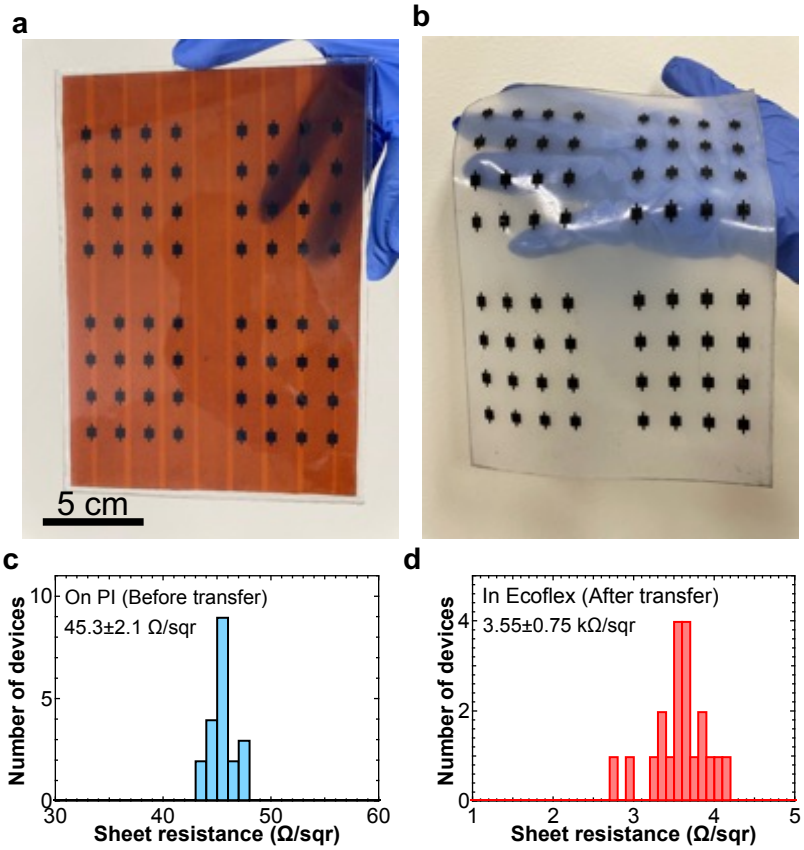

Figure S4. Photos of LIG (a) on the PI film and (b) in the ecoflex film. Histogram of sheet resistance (c) before and (d) after transfer.

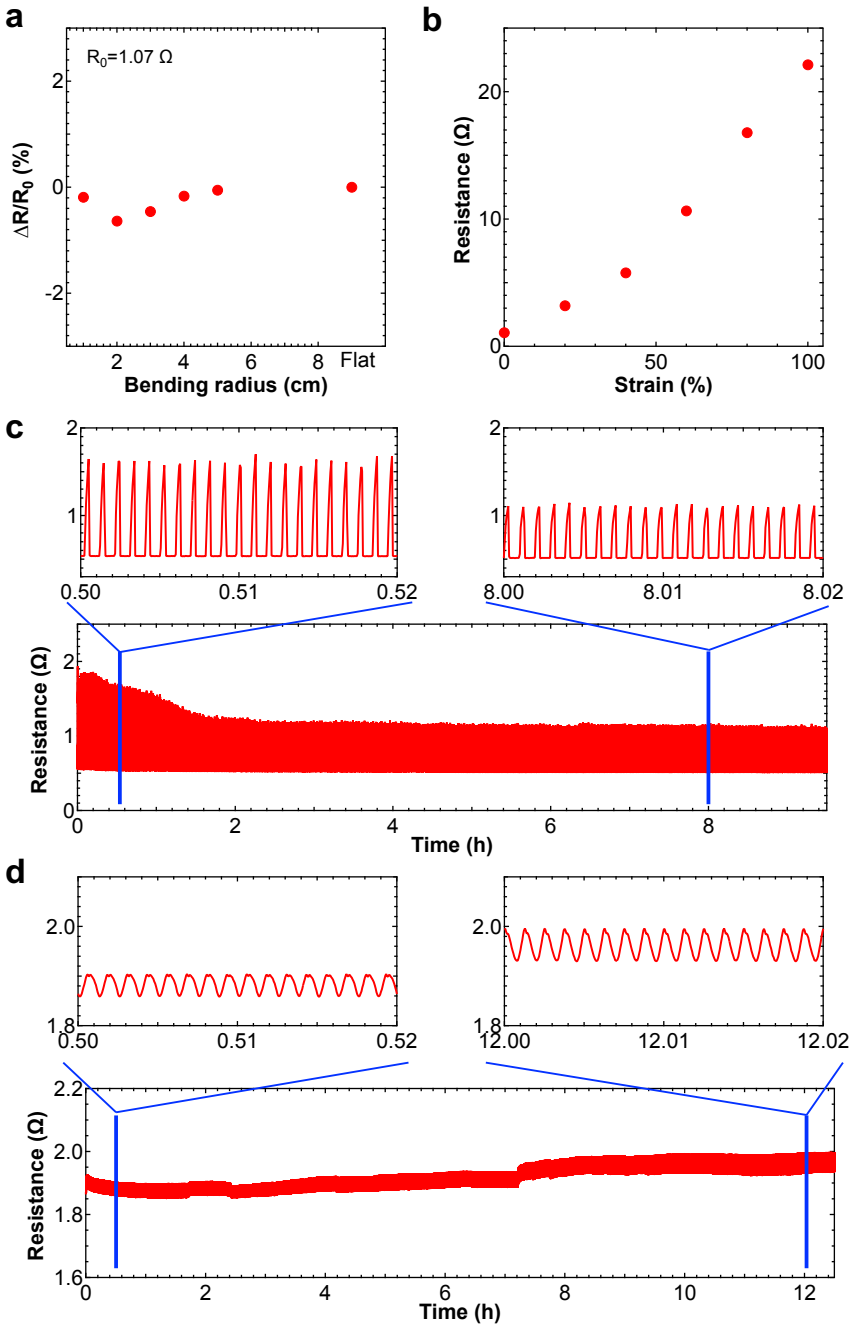

Figure S5. Electrical characteristics of liquid GaInSn, of the ecoflex/GaInSn/ecoflex structure. (a) Resistance change ratio at different bending radii. (b) Resistance at different tensile strains. Cycle tests when (c) pressure and (d) tensile strain by stretching were applied.

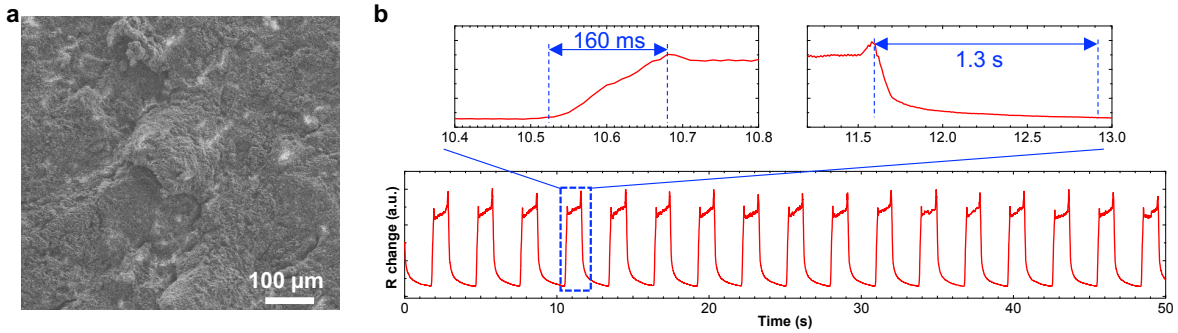

Figure S6. (a) SEM image of surface morphology of LIG/ecoflex after laser texturization. (b) Response time of the tactile pressure sensor measured by the sensor with texturization.

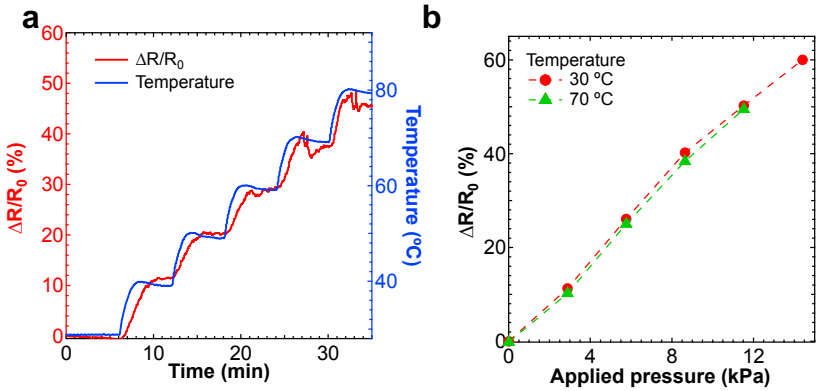

Figure S7. (a) Resistance change ratio at different temperatures. (b) Resistance change ratio as a function of applied pressure at 30 and 70 ºC.

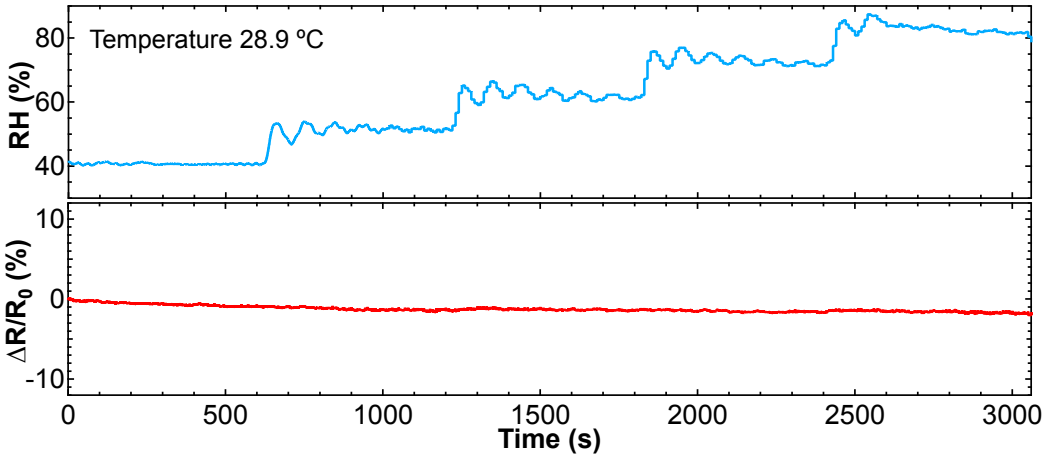

Figure S8. Resistance change ratio of the sensor at different relative humidities.

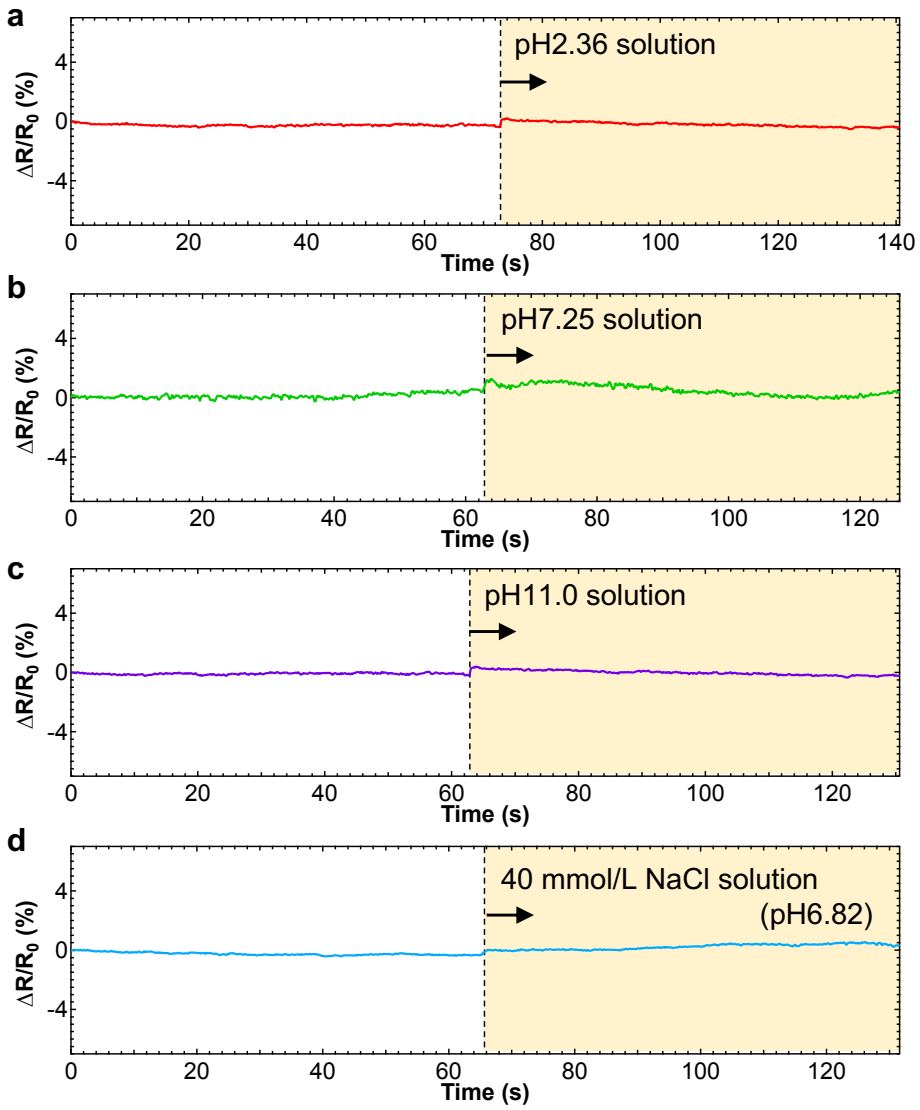

Figure S9. Resistance change ratio of the sensor in solutions at (a) pH 2.36, (b) pH 7.25, (c) pH 11.0, and (d) 40 mmol/L NaCl.

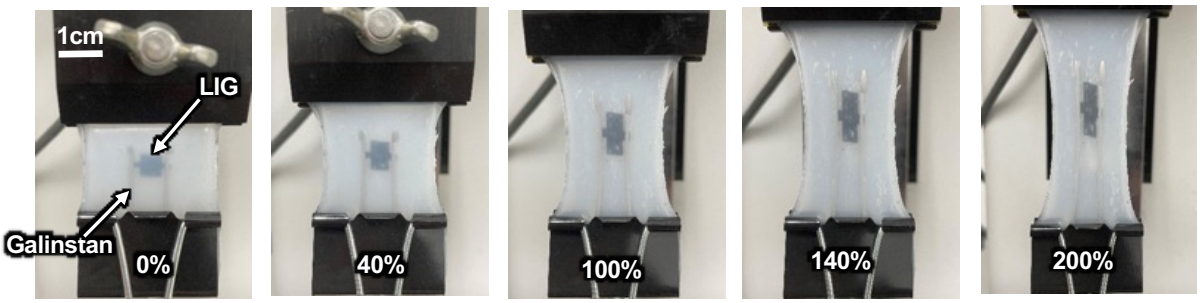

Figure S10. Photos of a pressure sensor at different degrees of stretching.

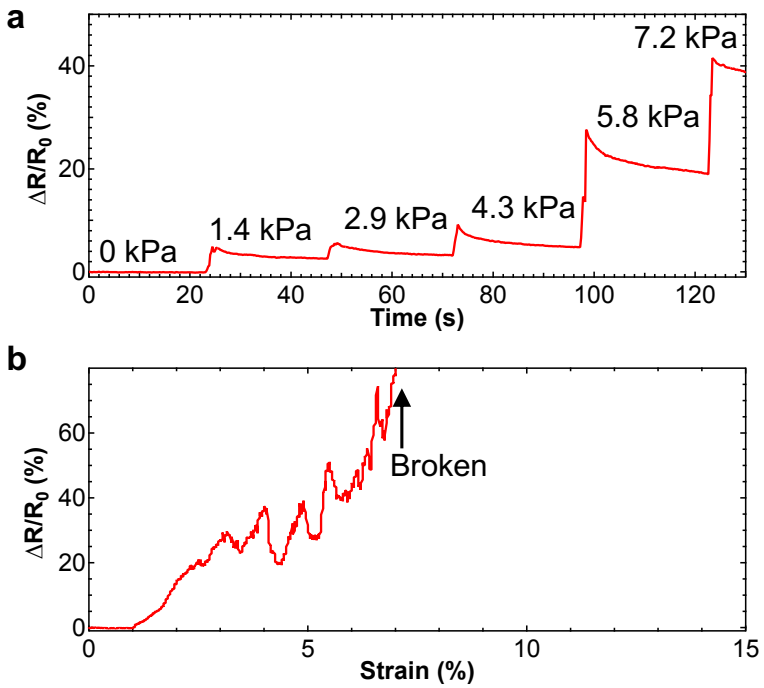

Figure S11. Resistance change ratio (a) at different applied pressures and (b) as a function of strain for the CB-based stretchable pressure sensor.

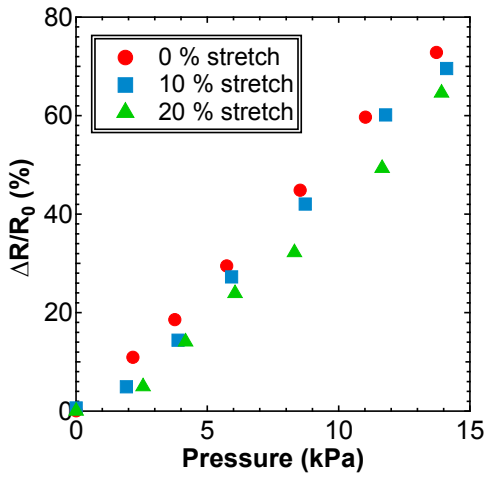

Figure S12. Resistance change ratio as a function of applied pressure at different stretching condition.

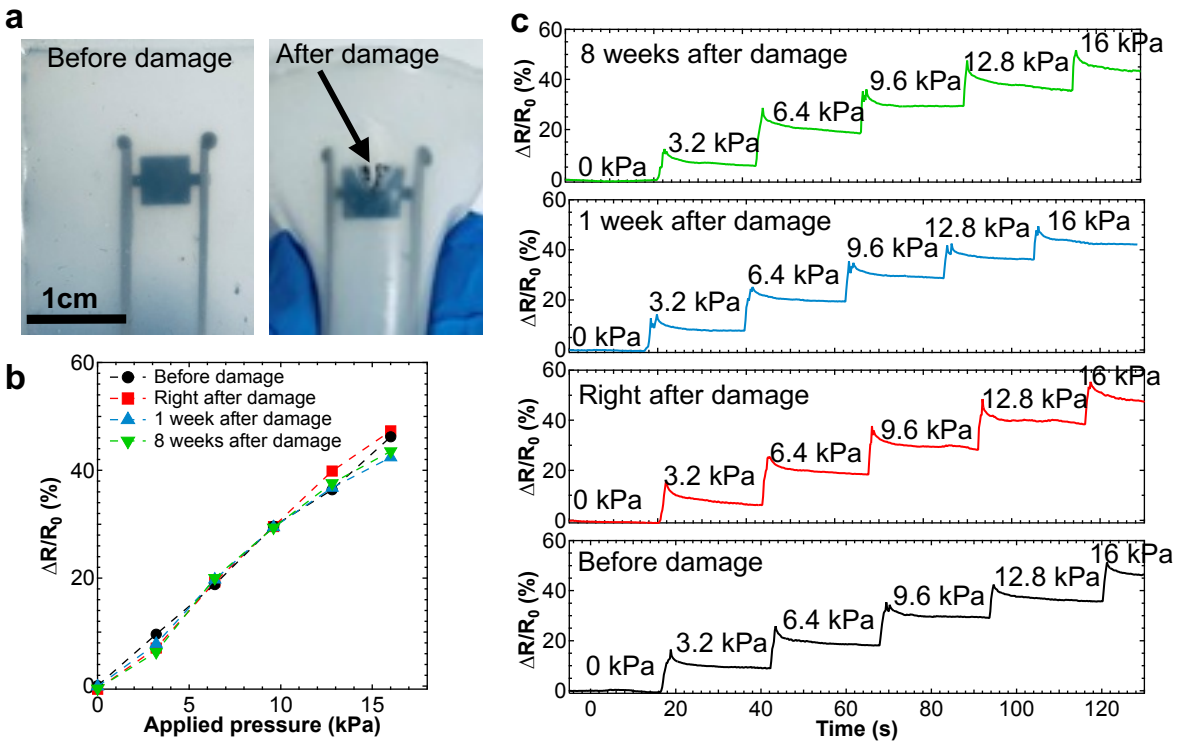

Figure S13. (a) Photos of a pressure sensor before and after damage. (b) Resistance change ratio and real-time resistance change ratio at different applied pressures before and after damage up to 8 weeks.

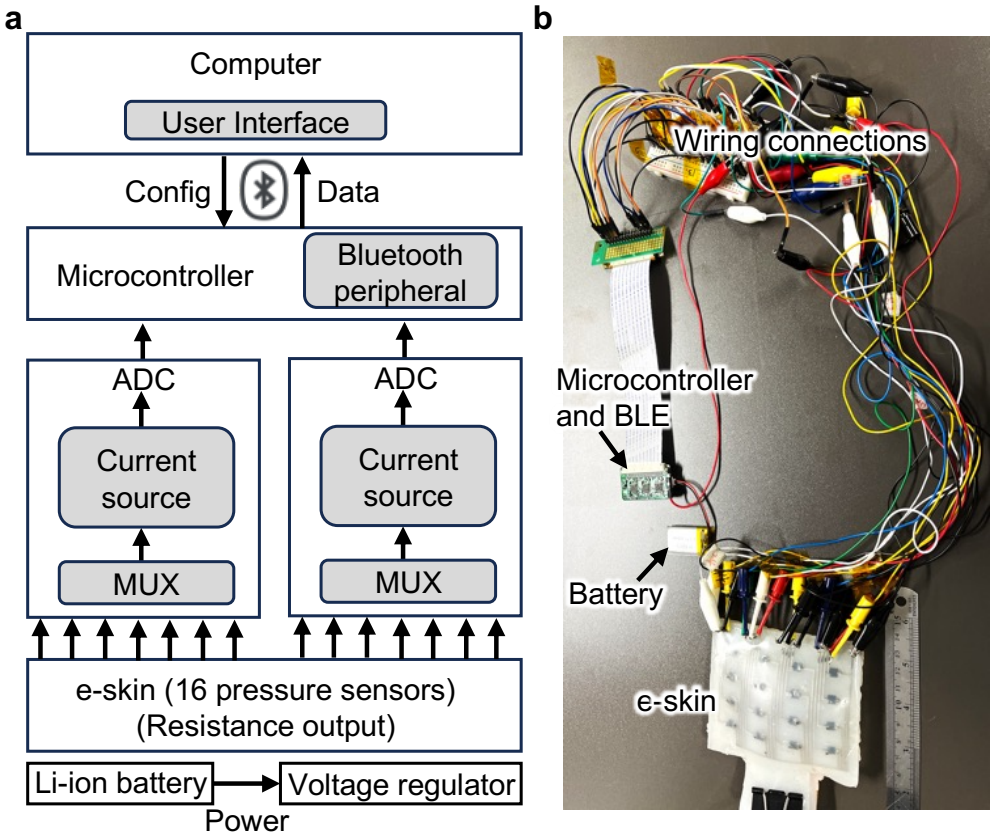

Figure S14. (a) Circuit diagram of the wireless system. (b) Photo of an e-skin with a wireless system.

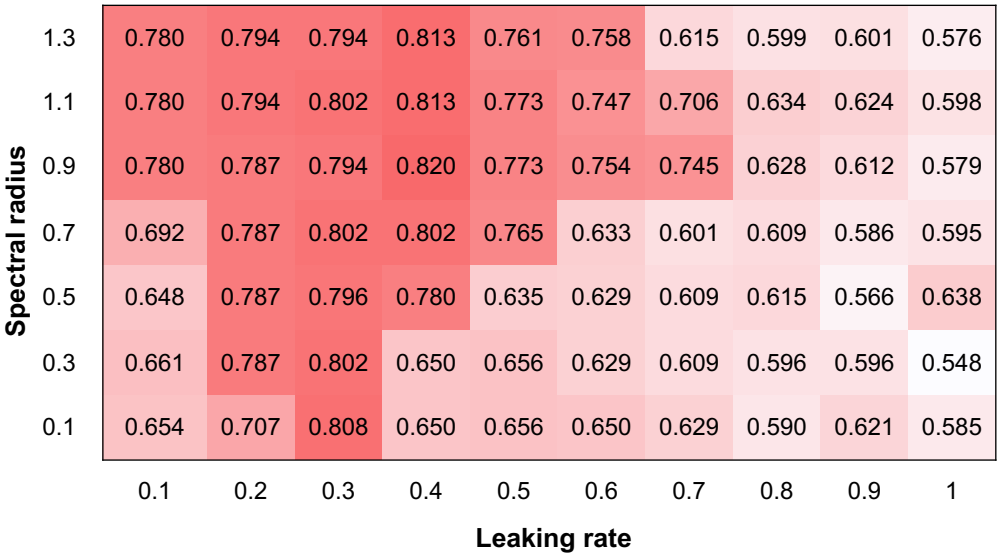

Figure S15. Grid search results of ESN at different spectral radii and leaking rates.

Table S1. Output accuracy using raw data (Raw) inputs and differential inputs with and without ESN.

	With ESN		Without ESN	
input	output1	output2	output1	output2
Raw value	0.555	0.996	0.339	0.994
Differential value	0.759	0.708	0.264	0.306

Table S2. Comparison of stretchable pressure sensors.

Materials	Sensitivity	Sensing Range	Stretchability	Response time	Cycle test	Stability after damage	Action recognition	Reference
mfaPDMS and BTO & PDMS	0.3 V/kPa (0-200 kPa) 0.05 V/kPa (200 kPa -800 kPa)	800 kPa	~ 187.32 %	44 ms	60000	Not reported	Not reported	Ref [1]
TPU/CNT	0.078 kPa^{-1} (0−6.5 kPa) 0.022 kPa^{-1} (6.5−16 kPa) 0.003 kPa^{-1} (16−55 kPa)	55 kPa	~ 160 %	300 ms	2500	Not reported	Not reported	Ref [2]
CB-doped silicone	-2.07 kPa^{-1} (0−20 kPa) -0.05 kPa^{-1} (20−150 kPa)	150 kPa	100 %	120 ms	7500	Not reported	Not reported	Ref [3]
PDMS-CNTs	0.15 kPa^{-1} (< 47 kPa) 0.08 kPa^{-1} (47 kPa-214 kPa) 0.04 kPa^{-1} (214 kPa-450 kPa)	450 kPa	~160 %	6 ms	10000	Not reported	Not reported	Ref [4]
prsIPDMS	18.94 kPa^{-1}	<40 kPa	50 %	284 ms	>5000	Not reported	Not reported	Ref [5]
PVDF/EMIM:TFSI /HMDA ionic elastomer	4.5 kPa^{-1} (0-1 kPa) 2.0 kPa^{-1} (1 kPa-10 kPa)	10 kPa	98 %	50 ms	>500	Not reported	Not reported	Ref [6]
Carbon mixture	4.8 %/kPa	18 kPa	50 %	Not reported	100	Not reported	Not reported	Ref [7]
LIG-ecoflex	2.73 %/kPa (0-80 kPa) 10.49 %/kPa (80 kPa-140 kPa)	140 kPa	>250 %	80 ms	10000	Stable	Yes	This work

References

[1] J. Yu, L. Chen, X. Hou, J. Mu, J. He, W. Geng, X. Qiao, X. Chou, *J. Materiomics* **2022**, 8, 247.

[2] G. Wang, M. Wang, M. Zheng, B. Ebo, C. Xu, Z. Liu, L. He, *ACS Appl. Nano Mater.* **2023**, 6, 9865.

[3] W. Kim, D. Kim, J. Kim, S. U. Park, H. K. Lee, J. Joo, S. G. Lee, J. W. Chae, J. Kim, S. Han, H. W. Baac, S. M. Won, *Adv. Mater. Technol.* **2023**, 8, 2300068.

[4] Y. Zhang, J. Yang, X. Hou, G. Li, L. Wang, N. Bai, M. Cai, L. Zhao, Y. Wang, J. Zhang, K. Chen, X. Wu, C. Yang, Y. Dai, Z. Zhang, C. F. Guo, *Nat. Commun.* **2022**, 13, 1317.

[5] Y. Zhang, Q. Lu, J. He, Z. Huo, R. Zhou, X. Han, M. Jia, C. Pan, Z. L. Wang, J. Zhai, *Nat. Commun.* **2023**, 14, 1252.

[6] Q. Su, Q. Zhou, Y. Li, Y. Chen, S.-Y. Teng, J. T. Kelleher, R. Nith, P. Cheng, N. Li, W. Liu, S. Dai, Y. Liu, A. Mazursky, J. Xu, L. Jin, P. Lopes, S. Wang, *Sci. Adv.* **2021**, 7, eabi4563.

[7] R. Matsuda, S. Mizuguchi, F. Nakamura, T. Endo, Y. Isoda, G. Inamori, H. Ota, *Scientific reports* **2020**, 10, 12666.